Available online at www.sciencedirect.com

ScienceDirect

Procedia CIRP 124 (2024) 358–361

www.elsevier.com/locate/procedia

13th CIRP Conference on Photonic Technologies [LANE 2024], 15-19 September 2024, Fürth, Germany

Understanding the thermo-fluid-microstructural impact of beam shaping in Laser Powder Bed Fusion using high-fidelity multiphysics simulation

Mohamad Bayat[a,*], Olga Zinovieva[b], Aleksandr Zinoviev[b], Richard Rothfelder[c], Karen Scharwzkopf[c], Michael Schmidt[c], Jesper H. Hattel[a]

[a] *Department of mechanical engineering, Technical University of Denmark (DTU), Building 425, 2800 Kgs. Lyngby, Denmark*
[b] *School of Engineering & IT, University of New South Wales Canberra, Canberra, Australia*
[c] *Lehrstuhl für Photonische Technologien, Friedrich-Alexander-Universität Erlangen-Nürnberg, Konrad-Zuse-Straße 3/5, 91052 Erlangen*

* Corresponding author. Tel.: +45 45254734; fax: +0-000-000-0000. *E-mail address:* mbayat@dtu.dk

Abstract

Beam shaping of lasers is a topic that has received relatively less attention in the context of metal additive manufacturing (MAM) processes. This technique allows for modulation or spatial alternation of the intensity profile of the laser. As the bulk of the work within MAM primarily revolves around Gaussian beam profiles, the precise impact and potential of other beam shapes is still an unanswered question. In this work a multiphysics numerical model of the laser powder bed fusion (LPBF) process of Ti6Al4V without powder is developed and the model can predict thermo-fluid-microstructural conditions. The model predictions are compared with experimental data from single-track specimens, and the comparison shows a very good agreement. It is shown that the ring spot beam profile (RSBP) results in substantially wider melt pools as compared to the ones forming using the Gaussian beam profile (GBP). The microstructural predictions show that for GBP the grains converge to the center line of the melt pool, while for ring beam profile (RBP), the grains tend to converge to a single point. Finally, the impact of different ring radii for RBP is studied and the results show that at larger ring radii, a noticeable bulge of liquid metal forms right beneath the laser beam.

Keywords: Beam shaping; laser powder bed fusion; multiphysics simulation; microstructural simulation; computational fluid dynamics

1. Introduction

It is well-established that MAM is one of the main pillars of the 4th industrial revolution but one of the remaining issues with MAM, is the very stochastic nature of these processes. With the aid of *in-situ* monitoring, Hamidi Nasab et al. [1] showed that the LPBF process can become highly unstable even if all process parameters are kept constant. Consequently, these instabilities would lead to defect formation over a wide range of length scales.

There are several conventional techniques to mitigate such defects and one of the most recognized methods is fine-tuning of process parameters or process parameters' variation. Apart from this, beam shaping (BS) is emerging as a new method to control and manipulate the melt pool shape and, as a result, the printed parts' morphology or microstructure. Depending on the level of complexity, the BS technology allows for spatial, temporal or spatio-temporal control over the beam intensity profile.

In temporal BS, as implied by its designation, certain on-and-off schemes are incorporated to modulate the laser power intensity temporally. This is typically done either via continuous laser power modulation via point-wise control of the laser beam. In spatial beam shaping, one can alter the intensity distribution of the laser beam over the focal plane. This is typically carried out via implementing adaptive optical elements (AOEs) [2] or with adjustable ring mode (ARM) lasers [3].

10.1016/j.procir.2024.08.133

Delving deeper into the subject of BS, one can subdivide spatial BS into two categories of process-induced BS and controlled BS. In the former type, the laser beam profile deviates from its targeted intensity profile due to the misalignment of the laser beam axis with respect to the vertical axis. Such process-induced or unintended BS typically takes place over the base plate corners in LPBF where the irradiation site is furthest from the center of the base plate, under which circumstance the laser beam can remain perpendicular, thus circular in shape. There have been a number of recent experimental and numerical works on the subject of unintended BS and they all report noticeable reduction in the melt pool depth and this, looking from a macroscopic point of view, brings about imperfect surface conditions.

On the other hand, in intended or controlled BS, one can alter the spatial distribution of the laser beam's intensity profile via AOE or ARM. Some recent experimental and numerical works have focused on applying elliptical beam shaping for obtaining site-specific microstructures [4]. According to [4], transverse-elliptical BS results in finer grains with an increased likelihood of obtaining equiaxed grain morphologies, and this was ascribed to the lower temperature gradients forming under such beam patterns. In two numerical works [5,6] the impact of BS was investigated during conduction laser welding and LPBF, respectively. As a downside, [5] only looked into stable melt pool conditions and [6] modelled the melt pool with a conduction-based thermal model. Despite the sheer number of simulation works within LPBF [7], only a handful of them are dedicated to the BS subject. Hence, an advanced deposition-scale model that simulates the thermo-fluid-microstructural evolution within the melt pool is kind of missing in the literature.

In this respect, we have come up with a simulation platform to model the thermo-fluid-microstructural conditions of the melt pool during spatial BS in LPBF. Two models are therefore developed in this work, one at deposition-scale, which predicts the melt pool's thermo-fluid conditions, and one at micro-scale, which simulates the grain growth at a lower dimension, and these two models are linked via a proper multi-scaling method. The rest of the paper is arranged in this order: the experimental and modelling setups are described in section 2 and then the results and discussion revolving around validation and a parametric study on the role of ring beam's radius are presented in section 3. Finally, the conclusion of the work is presented in the last section.

2. Experiments and modelling methods

2.1. Experiments

Several single track specimens were manufactured on top of a plane plate made of Ti6Al4V. Beam shaping was triggered by the AFX1000 (nLight, US) which was incorporated into the LPBF machine, SLM280HL (Nikon SLM Solutions, Germany). The system is capable of providing a laser wavelength of 1070 nm and the AFX1000 laser system can handle different beam profiles which are essentially a combination of GBP and RBP. The laser power and the scanning speeds for the specimens were set to 500 W and 1000 mm.s^{-1} in this work.

2.2. Deposition scale simulation

In this study, the heat and fluid flow conditions within the melt pool are predicted by a deposition-scale model. The model and its material properties (Ti6Al4V) are based on the previous works of the author group [8] with further modifications to allow for different beam shapes. The following conservation equations are solved to find the temperature and velocity vector field along with the surface conditions of the melt pool.

$$\frac{\partial \rho \alpha_i}{\partial t} + \frac{\partial}{\partial x_j}\left(\rho u_j \alpha_i\right) = \dot{S}_{\alpha_i}''' \tag{1}$$

$$\frac{\partial \rho u_i}{\partial t} + \frac{\partial}{\partial x_j}\left(\rho u_j u_i\right) = -\frac{\partial p}{\partial x_i} + \mu \nabla^2 u_i + \dot{S}_u''' \tag{2}$$

$$\frac{\partial \rho h}{\partial t} + \frac{\partial}{\partial x_j}\left(\rho u_j h\right) = k\frac{\partial}{\partial x_j}\left(\frac{\partial T}{\partial x_j}\right) + \dot{S}_T''' \tag{3}$$

Equations (1) and (2) described the mass and momentum balance respectively. α_i (-) is the phase fraction function, u_j (m s^{-1}) is velocity vector and S_u (N m^{-3}) is the volumetric source that entails the solidification drag forces, the buoyancy force, the Marangoni effect, capillarity and finally the recoil pressure term. Equation (3) expresses the energy balance in the system and in this model, a linear solidification rule is implemented.

T (K), k (W m^{-1} K^{-1}) and h (J kg^{-1}) are temperature, thermal conductivity and enthalpy (that involves the latent heat of fusion) in equation (3). The thermal source term S_T (W m^{-3}) contains convection heat transfer, radiation heat transfer, evaporation and finally, the laser heat flux contribution. The implemented laser heat flux is described by

$$\dot{q}_{laser}'' = I\left[\frac{\eta P}{\pi a^2} e^{-\frac{r^2}{a^2}}\right] + (1-I)\left[\frac{\eta P}{4\pi \varpi R r_0} e^{-\frac{(r-R)^2}{r_0^2}}\right] \tag{4}$$

In equation (4), the beam indicator I (-) determines the contribution from GBP and it ranges between zero and unity, where zero results in RBP and unity leads to GBP, respectively. In this equation, a (m), R (m), r_0 (m), and ϖ (-) stand for the central Gaussian beam's radius, ring radius, the Gaussian radius of the ring, and finally, the power scaling parameter.

2.3. Micro-scale simulation

In this work the micro-scale simulation for predicting the grain growth is carried out based on the cellular automata (CA) method and it receives interpolated data from the deposition scale model detailed in 2.2. The mesh size for the deposition scale model is set to 5 µm and the CA mesh is 1 µm which is sufficient to resolve grain features in LPBF. In the implemented CA method, each CA cell can have four states of liquid, undercooled liquid, interface and finally solid. Further information regarding the details of this model can be found in [7, 9]. Calculated temperature data from the deposition scale model are extracted from the mid-plane perpendicular to the scanning path and then fed to the CA code for grain simulation.

3. Results and discussion

3.1. Validation

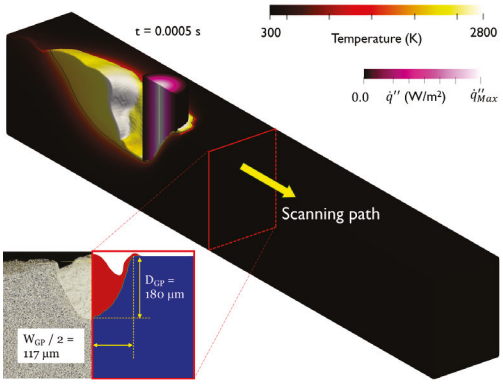

Fig. 1. Temperature contour and cross-sectional view of the track for GBP.

Fig. 1 shows the three-dimensional temperature contour of the melt pool forming under the influence of GBP along with the comparison between the experimental and numerical cross-sectional view of the melt track.

According to Fig. 1, due to the significant recoil pressure caused by the concentrated heating with GBP, a noticeable depression zone is formed right below the center of the laser beam. It is worth noting that the cross-section is made after the end of the process. This melt pool shape with the noted depression zone is widely observed in literature where GBP is employed. Details of the melt pool dimensions are given in Table 1. According to this table, there is an error of 4% and 11.1% in predicting the melt pool width and depth using GBP.

Table 1. Experimental and numerical track dimensions for GBP.

Validation	MP width (µm)	MP depth (µm)	Width/depth (-)
Experiment	225	200	1.30
Simulation	234	180	1.13
Deviation (%)	4.0%	10.0%	13.46%

The deviation noted in Table 1 could be due to uncertainties in the measured material properties and imperfect mismatch between the theoretical and implemented laser profiles.

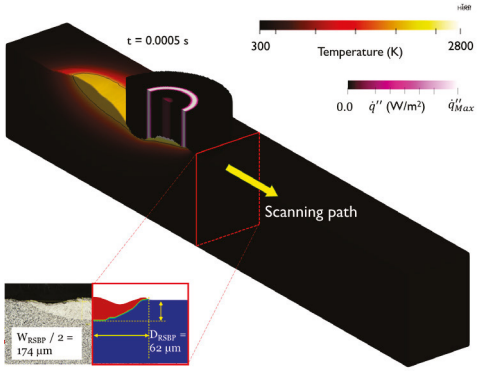

Fig. 2. Temperature contour and cross-sectional view of the track for RSBP.

Fig 2 shows the predicted melt pool temperature using the ring spot beam profile (RSBP) along with the comparison between the experimental and numerical track cross-sections.

Based on Fig. 2, the melt pool using RSBP is substantially wider and at the same time shallower than the one formed under GBP, similar observations were reported in [10]. The reason for this is the lowered heat flux intensity due to the larger laser area. Details of this comparison are given in Table 2.

According to Table 2, the predicted melt pool depth is in a perfect agreement with the experimental value whereas the simulated melt pool width is 5.18% smaller than in the experiment. The experimental melt pool measurements are averaged for 5 similar tracks made with identical process parameters.

Table 2. Experimental and numerical track dimensions for RSBP.

Validation	MP width (µm)	MP depth (µm)	Width/depth (-)
Experiment	367	62	5.92
Simulation	348	62	5.61
Deviation (%)	5.18%	0.00%	5.18%

The reason for a better agreement between the experimental and predicted melt pool dimensions under RSBP is the fact that under this beam shape, laser heat flux is substantially lower than in GBP and this leads to more stable melt pool without strong recoil pressures that could potentially lead to keyhole undulations.

3.2. Impact of ring beam on grain morphology

To better understand the impact of beam shaping on the microstructural conditions, two deposition-scale simulations were done, one with GBP and the other with RBP with 250 W and 700 mm.s^{-1} laser power and scanning speed, respectively. The ring and central Gaussian radii are set to 100 µm and 42 µm, respectively. The predicted grain morphologies for GBP and RBP are displayed in Fig. 3. The initial grain sizes for running the CA simulation were set to 30 µm.

According to Fig. 3., the grains for GBP have grown and converged to the centerline of the melt pool and for the case of RBP, the grains seem to have converged to a single point right on the top center of the melt pool. The convergence of the grains towards the centerline of the melt pool is widely observed in keyhole melt pools in laser welding and LPBF. On the other hand, according to Fig. 3 (b), the grains seem to

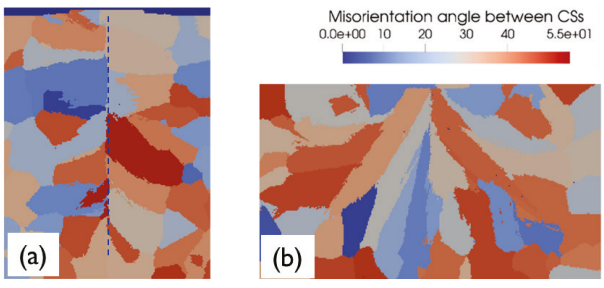

Fig. 3. Predicted grain morphology and misorientation angle for (a) GBP and (b) RBP. The ring radius for RBP is 100 µm. Welding direction is normal to the contour plane towards outside.

have converged to a point in the case for RBP.

3.3. Impact of ring beam radius

Another parametric study is carried out to discover the impact of ring beam radius on the melt pool conditions. Therefore, the parametric study in section 3.2. is partially extended by running three extra cases with intermediate ring beam radii of 80 µm, 60 µm and 40 µm. The calculated temperature contours of the melt pools for these three additional cases are shown in Fig. 4 along with their associated track cross-sections.

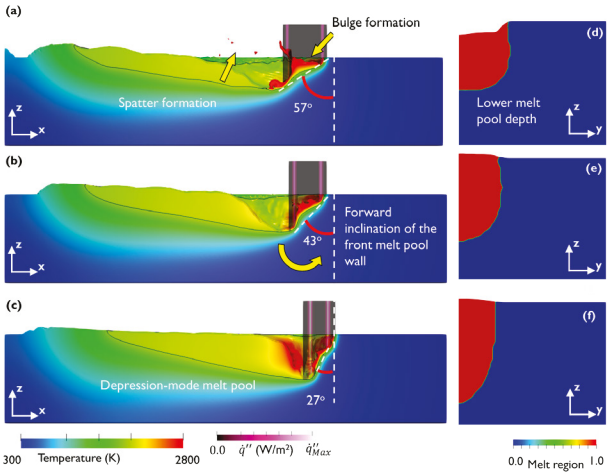

Fig. 4. Side view of the melt pool temperatures for ring radii; (a) 80 µm, (b) 60 µm and (c) 40 µm along with their corresponding single track profiles shown in (d) – (f).

According to Fig. 4 (a), the ring radius of 80 µm has led to an apparent bulk formation in the center of the laser beam where the laser intensity is zero. In this situation, the irradiated zones which are subject to the laser beam heating undergo noticeable recoil pressures with an annular-like shape. Because of this annular depression zone, the material is displaced to the center of the melt pool right underneath the spot in which the laser beam intensity is zero. This would then lead to bulge formation in the middle of the melt pool. Furthermore, as the surface tension decreases with temperature, the material in the center of the melt pool loses its ability to contain the liquid metal bulge and this results in significant spatter formation, see Fig. 4 (a). By decreasing the ring radius, according to Fig. 4, one can notice that the bulge formation is nearly avoided due to well-overlapped beam radiation leading to no zero-radiation zones. Moreover, due to more concentrated heating taking place under ring radii of 40 µm and 60 µm, the depression zone which is closely linked to evaporation and likewise temperature, becomes more significant and this brings about deeper melt pools which resembles the ones forming with GBP.

4. Conclusion

In this work a multiphysics numerical model of the LPBF process of Ti6Al4V alloy is developed to study the impact of beam shaping on the thermo-fluid-microstructural conditions of the melt pool. Dedicated experiments including single track specimens are manufactured with RSBP and GBP for comparison with the multiphysics model. The comparison between the experimental and predicted melt pool profiles shows a very good agreement, hence confirming the validity of the developed model. It is noted that RSBP leads to wider melt pools, and this paves the way for a lower number of hatches, which is necessary for boosting the production rate in LPBF. The microstructural simulation carried out with the CA method shows that with GBP the grains converge to the center line of the melt pool while for RBP the grains tend to converge to a single point on the surface of the sample. Finally, a parametric study is performed where it is observed that reducing the ring radius leads to melt pools with larger depth-to-width ratio – similar to the ones observed for GBP.

Acknowledgment

Mohamad Bayat acknowledges receiving funding from the Danish-funded project microAM funded by Villum fonden (MicroAM-VIL54495). Jesper Hattel received funding from the Horizon Europe CL4 project 101138289, GlobalAM.

References

[1] Nasab, M. et al., Operando X-Ray imaging of stochastic inter-regime instabilities in laser melting processes: direct evidence of acoustic emission signatures, Nat Commun (2023).
[2] Salter, P.S., Booth, M. J. Adaptive optics in laser processing, Light Sci Appl 8 (2019).
[3] Md. pour, M. et al., Adjustable ring mode and single beam fiber lasers: A performance comparison, Manuf Lett 25 (2020)
[4] Shi, R. et al., Microstructural control in metal laser powder bed fusion additive manufacturing using laser beam shaping strategy, Acta Mater 184 (2020) 284–305.
[5] Ebrahimi, A., Revealing the effects of laser beam shaping on melt pool behavior in conduction-mode laser melting, Journal of Materials Research and Technology 27 (2023) 3955–3967.
[6] Moore, R., Microstructure-Based Modeling of Laser Beam Shaping During AM, JOM 76 (2024) 1726–1736.
[7] Bayat, M., et al., Holistic computational design within additive manufacturing through topology optimization combined with multiphysics multi-scale materials and process modelling, Prog Mater Sci 138 (2023).
[8] Charles, A., Elucidation of dross formation in laser powder bed fusion at down-facing surfaces: Phenomenon-oriented multiphysics simulation and experimental validation, Addit Manuf 50 (2022).
[9] Zinovieva, O. et al. Elastic properties of additively manufactured steel produced with different scan strategies, Int J Mech Sci 244 (2023) 108089.
[10] Cloots, M. Uggowitzer, P.J. , Wegener, K. Investigations on the microstructure and crack formation of IN738LC samples processed by selective laser melting using Gaussian and doughnut profiles, Mater Des 89 (2016) 770–784